

Re-entrant transition as a bridge of broken ergodicity in confined monolayers of hexagonal prisms and cylinders

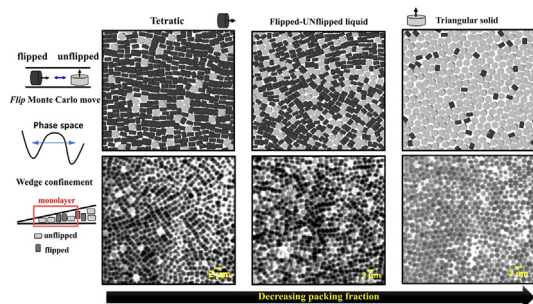


B.P. Prajwal^a, Jen-Yu Huang^a, Meera Ramaswamy^b, Abraham D. Stroock^a, Tobias Hanrath^a, Itai Cohen^b, Fernando A. Escobedo^{a,*}

^a Department of Chemical and Biomolecular Engineering, Cornell University, Ithaca, NY 14853, USA

^b Department of Physics, Cornell University, Ithaca, NY 14853, USA

GRAPHICAL ABSTRACT



ARTICLE INFO

Article history:

Received 23 July 2021

Revised 8 September 2021

Accepted 13 September 2021

Available online 15 September 2021

Keywords:

Anisotropic colloids

Re-entrant phase transition

Monolayer confinement

Self-assembly

ABSTRACT

The entropy-driven monolayer assembly of hexagonal prisms and cylinders was studied under hard slit confinement. At the conditions investigated, the particles have two distinct and dynamically disconnected rotational states: unflipped and flipped, depending on whether their circular/hexagonal face is parallel or perpendicular to the wall plane. Importantly, these two rotational states cast distinct projection areas over the wall plane that favor either hexagonal or tetragonal packing. Monte Carlo simulations revealed a re-entrant melting transition where an intervening disordered Flipped-Unflipped (FUN) phase is sandwiched between a fourfold tetratic phase at high concentrations and a sixfold triangular solid at intermediate concentrations. The FUN phase contains a mixture of flipped and unflipped particles and is translationally and orientationally disordered. Complementary experiments were conducted with photolithographically fabricated cylindrical microparticles confined in a wedge cell. Both simulations and experiments show the formation of phases with comparable fraction of flipped particles and structure, i.e., the FUN phase, triangular solid, and tetratic phase, indicating that both approaches sample analogous basins of particle-orientation phase-space. The phase behavior of hexagonal prisms in a soft-repulsive wall model was also investigated to exemplify how tunable particle-wall interactions can provide an experimentally viable strategy to dynamically bridge the flipped and unflipped states.

© 2021 Elsevier Inc. All rights reserved.

1. Introduction

Assemblies of colloidal particles have promising functional applications as active constituents of photovoltaic devices [1], optical films [2], and catalysts [3]. Recent advances in the synthetic and

* Corresponding author.

E-mail address: fe13@cornell.edu (F.A. Escobedo).

fabrication approaches of faceted sub-micron particles with different shapes have spurred interest in using these particles as basic building blocks for the assembly of targeted complex structures. The type of order and symmetry of these structures can be tuned by controlling such properties as particle geometry [4,5], interparticle interactions (e.g., chemical patchiness) [5], depletion forces [6–8], and external fields including hard/soft wall confinement [9–13]. Entropic and external forces play a crucial role in the assembly of nanoparticles, and their interplay is being systematically delineated by studies that focus on the effects of each driving force separately.

A large variety of superstructures arises when polyhedral colloidal particles are assembled at fluid interfaces [14] or inside confined geometries such as within parallel hard plate/wedge cell [10,15], spherical [16,17], or square cavities [18]. The confinement effects can drastically change the phase behavior of the system and be dominant when only a few particle layers can be accommodated along at least one direction. For hard spheres, for example, in contrast to the single isotropic to crystal phase transition in the bulk, a rich phase behavior was observed when confined between two parallel hard plates as the plate separation was varied to only accommodate one-to-a-few particle layers [9]. Numerous computational and experimental investigations have been carried out to explore the phase transitions in slit confinement with a variety of particle shapes, including members of the truncated cubes family [10], spherical or mushroom caps [12,19], hard rectangles [20], hard rods [18], hard platelets [21], and dimers [13,22,23]. The results from these studies have provided an understanding of the combined effects of particle anisotropy and confinement length. An interesting attribute associated with the parallel slit confinement model is that it allows access to the two-dimension (2D) and quasi-2D behavior by just altering the confinement separation: The phase behavior can drastically change depending on the particles' accessibility to rotational and translational states across the gap.

This work is focused on mapping the thermodynamic phase behavior of two anisotropic convex shaped particles; namely, hexagonal prisms (HPs) and cylinders (CYLs), under parallel slit confinement with hard and soft-repulsive walls. The geometry of these shapes is such that the flipped and unflipped particle orientations cast two different projected areas and shapes (Fig. 1) against the confinement wall. The flipped and unflipped orientations correspond to the particle with its side parallel and perpendicular to the wall plane, respectively (see Fig. 1). Using the hard confinement model, this scenario imposes a hindrance to the different possible rotational and translational states that the particles can populate during self-assembly. By carefully choosing the confinement and the particle dimensions, we can create disconnected regions in the rotational phase space between the flipped and unflipped orientations that cause a non-ergodic dynamic behavior in the system. In simulations, we overcome this dynamic broken ergodicity by using unphysical specialized Monte Carlo (MC) moves that effectively sample all regions of phase space. These MC moves allow particles to transition between flipped and unflipped states, akin to changing the “type” of particle in a two-component system, categorized by the projected 2D geometry: hexagon \leftrightarrow rectangle for the HPs, and disk \leftrightarrow rectangle for the CYLs. Crucially, the transition between these two orientations also provides a mechanism to switch between structures with different packing symmetry and/or lattice spacing. The hexagonal projections of unflipped HPs exhibit a KTHNY-type [24] phase transition with a continuous fluid-hexatic transition and a continuous hexatic-solid transition [25]. Likewise, the disk-shaped projections of the unflipped CYLs have a first-order fluid-hexatic transition and a continuous hexatic-solid phase transition [26]. In contrast, the rectangular projections of flipped HPs and CYLs exhibit a two-

stage KTHNY transition with the continuous fluid-tetratic and a continuous tetratic-tetratic solid transitions [27]. The tetratic and hexatic phases are partially ordered phases characterized by a short-range translational order and quasi-long ranged bond orientational order. The tetratic solid phase has long-range translational and bond orientational order.

A challenge associated with the assembly of anisotropic particles in confinement lies in the ability to sample their equilibrated quasi-2D positions and orientations. A “soft” confinement model is proposed in this work as a way to overcome the broken ergodicity by allowing the system to dynamically bridge the flipped and unflipped particle orientations, but tunable external fields could also be used to control the confinement forces. For instance, application of external electric fields has proven to be an effective approach to manipulate particle assemblies where the relative polarizability of the particle and the solvent medium controls the particle position, and the relative polarizability of each particle axis controls the particle orientations [28]. For bulk 3D system, a switching transition between the body-centered cubic crystal to a partially ordered plastic crystal structure was achieved for charged rod-like colloidal particles by tuning the electric field [29]. A wide range of structures with hexagonal and tetratic-like symmetries and string fluids were obtained for platelets subjected to varying electric field strengths and confinement separations that allowed particles to access flipped and unflipped orientations [30].

Our simulations predict a re-entrant transition for the HPs and CYLs in hard confinement where an intervening disordered phase occurs between two solid phases: a high-density tetratic phase and a low-density triangular solid (1Δ) phase. We termed this disordered phase as the Flipped-Unflipped (FUN) phase due to the mixture of flipped and unflipped orientations, high particle mobility, and significant degree of disorder. Indeed, the FUN phase has local clusters of flipped and unflipped particles with incompatible footprint areas that are distributed randomly throughout the simulated domain. At narrow separations, we observed a first order transition between the tetratic phase and the 1Δ phase for both HPs and CYLs. In our athermal system, different phases result from the interplay between pressure \times volume contributions to the free-energy, which generally favors denser structures at high pressures, and the particles' rotational and translational contributions to the entropy which strongly depend on gap separation. By varying the density and confinement separation, we can tune regions of phase space accessible to the dispersion with our MC moves and experimental preparation. MC simulations were also carried out for poly-disperse CYLs in hard confinement to allow comparison of the predicted structures with tetratic, FUN, and 1Δ phases obtained experimentally by assembling fabricated CYLs in a wedge cell confinement. The consistency in the structural characteristics of the assembled phases obtained in experiments and simulations is attributed to both methods being able to comprehensively sample the accessible orientational phase space. Particles in the wedge confinement cell are able to dynamically explore their flipped and unflipped states at wide separations, and as they migrate to the narrow separations, rearrange laterally to pack more densely; particles in the MC simulations are able to ergodically sample both orientational states through specialized moves at all conditions. Thus, experiments and simulations produce assembled phases that have similar fraction of flipped/unflipped particles although not necessarily at the exact same confinement conditions (i.e., concentrations), hence providing comparable access to a variety of otherwise disconnected regions of phase space. The re-entrant FUN phase was also observed for HPs simulated in a soft confinement model where a finite transition barrier allows dynamic switching between flipped and unflipped orientations.

The outline of this paper is as follows. Section 2 details the hard and soft confinement models, simulation method, and the experi-

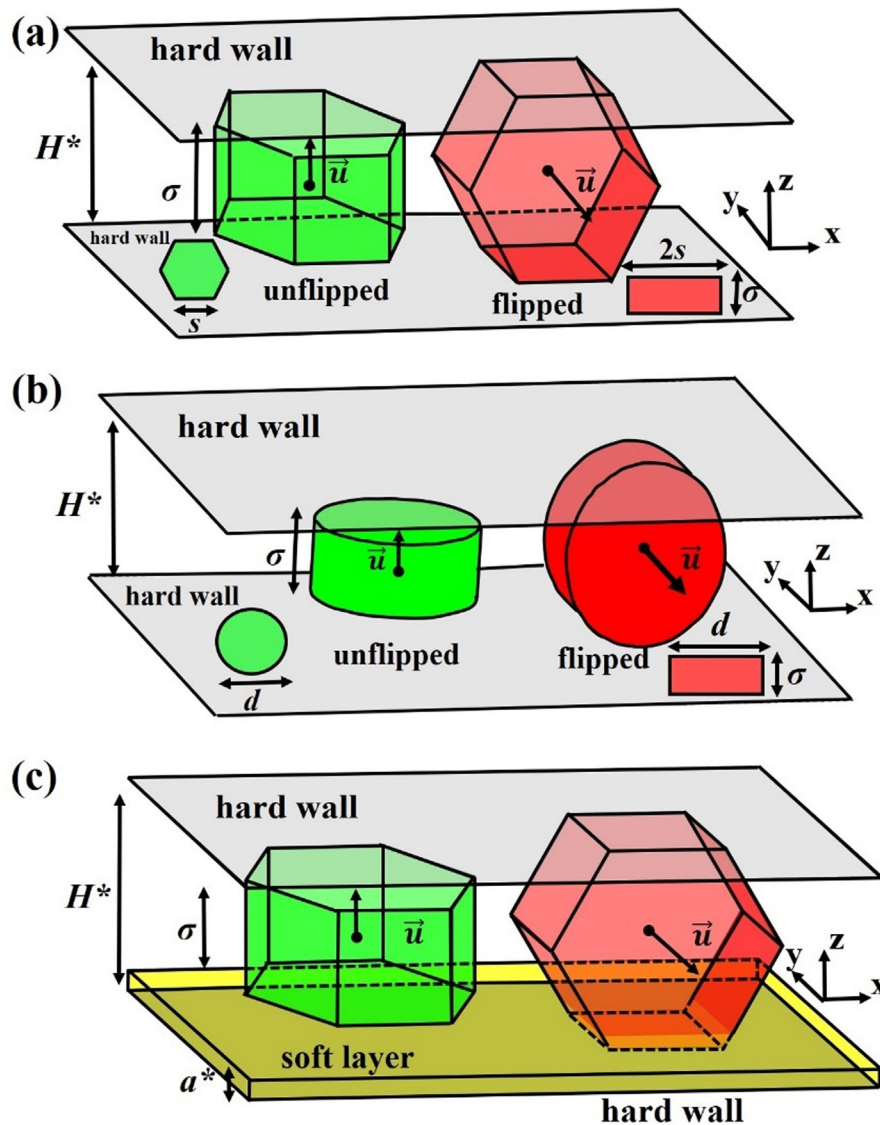


Fig. 1. Schematic of slit-confinement simulation model with (a,b) hard and (c) soft-repulsive walls. H^* is the separation between the hard walls scaled with respect to the height of the particle σ . The flipped (in red) and unflipped (in green) orientations and 2D projected geometries are shown for (a) HPs, and (b) CYLs. The particle's principal orientation unit vector, \vec{u} , is parallel/perpendicular to the XY plane when flipped/unflipped. s is the edge length of the hexagon face in HP, d is the diameter of the circular face in CYL. In (c) a^* is the thickness of the soft layer scaled with respect to σ . (For interpretation of the references to colour in this figure legend, the reader is referred to the web version of this article.)

mental protocol to fabricate the CYL colloids and assembling them in the wedge cell confinement. Section 3 describes various order parameters used to characterize the phase transitions. Sections 4.1/4.2 present summary/detailed description of the phase behavior of HPs and CYLs under hard wall confinement, Section 4.3 discusses the effect of size dispersity and a comparison between the simulated and experimental structures, and Section 4.4 presents simulation results for HPs under the soft confinement model. Finally, Section 5 presents closing remarks and an outlook of our study.

2. Methodology

2.1. Simulation model and protocol

Simulations of N hard anisotropic particles under parallel plate confinement were carried out using the standard Metropolis Monte Carlo algorithm in an isothermal-isobaric (NPT) ensemble.

Fig. 1 shows the hard wall and soft confinement models that corresponds to a case without and with a soft layer of varying thickness, $a^* = a/\sigma$, where σ is the height of the particle. The scaled plate separation is $H^* = H/\sigma$, where H is the distance between the hard walls. We simulated a range of H^* values (imposing periodicity in XY plane) that accommodates only a single particle layer. The aspect ratio of the particles, $R = b/\sigma$ is fixed by varying the characteristic length b , where $b = 2s$ for HPs and $b = d$ for CYLs. s is the edge length of the hexagonal face in the HP and d is the diameter of the circular face in the CYL. The R values chosen for the hard confinement model are 2 for HPs and 1.574 for CYLs and the phase behavior was mapped for $H^* = 1.0$ –1.9 for HPs and $H^* = 1.582$ –1.61 for CYLs. We observed a quasi-2D phase behavior at $H^* > 1.74$ for HPs and $H^* > 1.574$ for CYLs, where the plate separations are such that the particles can access both flipped and unflipped orientations. The range of H^* values chosen is such that the flipped and unflipped orientations are dynamically disconnected (see Sec. I in the [supplementary information](#), SI). The two orientations are

distinguished based on the $|\vec{u} \cdot \vec{z}|$ values where \vec{u} is the principal orientation unit vector of the particle and \vec{z} is the unit vector in z direction (see Fig. S1 in the SI). When flipped the \vec{u} is parallel to the wall and perpendicular to the wall when unflipped (see Fig. 1). For the soft confinement model, we set $R = 1.82$ and $H^* = 1.95$ to allow for the dynamic (or continuous) rotation of the HPs between the flipped and unflipped orientations. These R values are chosen such that they satisfy two geometric constraints: (i) The particles can access both flipped and unflipped orientations at the confinements that only allow formation of monolayers; (ii) The unflipped orientation projects a larger hexagonal/circular area than the rectangular area projected by the flipped orientation. The R values chosen for our study are just representative, but we expect similar trends in phase behavior for HPs and CYLs with other R values that satisfy both geometric constraints.

We consider excluded volume interaction with the pair potential between the particles, $U(r_{ij})$, given as,

$$U(r_{ij}) = \begin{cases} \infty, & \text{if } r_{ij} < r_{ij}^{\max} \\ 0, & \text{otherwise} \end{cases} \quad (1)$$

where, r_{ij} is the distance between the particle center of mass, r_{ij}^{\max} is the maximum r_{ij} distance beyond which overlap cannot occur. The overlap between the particles is checked using the Gilbert-Johnson-Keerthi (GJK) algorithm [31]. The hard and soft repulsive potentials, $U(r_i)$, between the particle and the hard walls and between the particle and a soft-grafted layer is given by,

$$U(r_i) = \begin{cases} \infty, & \text{if } V_{o,hw}(r_i) \neq 0 \\ \beta V_{o,sw}, & \text{if } V_{o,sw}(r_i) \neq 0 \\ 0, & \text{otherwise} \end{cases} \quad (2)$$

where, r_i is the particle center of mass position, $V_{o,hw}$ and $V_{o,sw}$ are the volumes of the particle that overlap with the hard walls and soft grafted layer. In this simple soft repulsive potential model, a presumed grafted layer exists with tunable hardness modulus, $\beta^* = \beta\sigma^3$, and thickness a^* . Because of the particle shape anisotropy, the wall-particle interaction potential will depend in a complex way on not only the particle-wall distance but also the particle orientation. Model (2) above can be seen as a first approximation to a soft repulsive potential where the energy required to deform the soft grafted layer is proportional to the particle volume that overlaps with (and pushes out) the soft layer. The 3D simplices were constructed to compute $V_{o,sw}$ using the particle vertices and centroid [32]. The overlap between each particle and the hard walls was detected using the separating axis theorem [33].

For the hard confinement model, stepwise expansion/compression runs were carried out at each H^* value by equilibrating the system at each pressure step. These runs were used to map the phase behavior along the solid and liquid branches to detect any hysteresis present between expansion and compression. For the soft confinement model, we studied the phase behavior for HPs at $H^* = 1.95$ for varying a^* and β by performing compression runs and following the same procedure used for the hard confinement model. The dimensionless pressure is $P^* = P\sigma^3/k_bT$, where T is temperature and k_b is Boltzmann's constant. The equation of state was mapped by varying P^* and calculating the volume fraction, $\phi = NV_p/V$, where V_p is the volume of each particle, N is the number of particles and V is the system volume. To minimize finite size effects, we choose the initial system size to have a minimum of 15–35 particles per layer along X and Y dimensions. For the hard confinement model, 1254 and 1352 HPs were used for compression and expansion runs, and 1024 CYLs for both compression and expansion runs. For the system with soft confinement, 1254 HPs were used. We mapped the high-density solid branch of the phase diagram with the expansion runs and the intermediate and lower

density branch with the compression runs. At any H^* , the initial configuration for the compression runs is the isotropic phase and for the expansion runs is the densest crystal phase simulated using Floppy Box Monte Carlo algorithm [34].

At each pressure step, we perform 3×10^7 MC cycles with the last 5×10^6 cycles used for production runs, where each MC cycle consisted of N translational, N rotational, $N/10$ flip, $N/10$ two-particle in-plane rotation and 2 vol moves. All move sets obey detailed balance and the step size for the translational, rotational, and volume moves are adjusted to have acceptance probabilities of 0.4, 0.4, and 0.2. We incorporated flip moves that attempt to randomly orient a chosen particle in a plane that is perpendicular to its current orientation. The flip move was particularly important for our hard confinement model having broken dynamic ergodicity, as it helps to access the flipped and unflipped orientations that are difficult to sample with standard rotational moves. The two-particle in-plane moves improve ergodic sampling for high-density solid phases and were implemented as follows. First, two particles are chosen, the first randomly and the second its closest neighbor. Next, these particles are rotated in the XY plane about their combined center of mass (using z-component unit vector) by 90° (clockwise/anticlockwise) [22]. The move is accepted if: (i) the second particle is still the closest to the first one to maintain reversibility, and (ii) no overlap is incurred. Volume moves attempt changes in XY box area and shape (anisotropic moves) during the expansion runs, while only changes in XY area during compression runs.

2.2. Experimental protocol for fabrication of colloidal CYLs

We used a photolithographic procedure to fabricate colloidal CYLs from an epoxy-based negative photoresist, SU-8 2001 series, which provides high-throughput of different colloidal shapes within narrow size polydispersity [35,36]. The fabrication process includes three key steps: (i) Spin coating of the photoresist on top of a sacrificial Omnicore layer on a 100 mm silicon substrate. The thickness of the photoresist layer controls the height of the particles, σ . (ii) Exposure of the photoresist to ultraviolet light (*i*-line) through a Cr photomask with round holes to control the diameter, d of the particles. (iii) Development of the photopatterned resist layer and release of the particles by dissolution of the Omnicore layer. The particles were then washed with DI water and suspended in an aqueous solution of Tergitol NP70, a non-ionic surfactant that adsorbs on the surface of the particles and provides a steric barrier holding the particles outside the vdW attraction regime to prevent irreversible aggregation [35,37]. The thickness of the NP70 layer and the zeta potential of the particles were estimated by Badaire et al. [37] to be 8.2 ± 3.3 nm and -21.0 ± 6.2 mV, respectively. This route generated particles with $d = 1.56 \pm 0.08$ μm and $\sigma = 0.96 \pm 0.06$ μm and the suspension concentration $\sim 4.5 \times 10^8$ particles/ml. The size dispersity, s_d and s_σ in diameter and height were measured using the SEM micrographs and estimated to be 0.05 and 0.06, respectively. A more detailed description of the fabrication procedure and particle characterization is given in Sec. II of the SI. The suspension was transferred to a 10 ml glass vial and mixed with a small amount of fluorescein dye (2 mg/ml) to enable confocal imaging. Finally, the CYLs were assembled in the wedge cell confinement to study the organization of the particles using fast confocal microscopy (see Sec. IID in the SI).

3. Order parameters

3.1. Cubatic orientation order parameter

The global orientational order was measured using the cubatic order parameter, P_4 , which is defined as,

$$\begin{aligned} \langle P_4 \rangle &= \max_{\vec{n}} \frac{1}{N} \sum_i P_4(\vec{u}_i, \vec{n}) \\ &= \max_{\vec{n}} \frac{1}{8N} \sum_i (35 \cos^4 \theta_i(\vec{n}) - 30 \cos^2 \theta_i(\vec{n}) + 3) \end{aligned} \quad (3)$$

where \vec{u}_i is the principal orientation vector of the particle and the \vec{n} is the director that maximizes $\langle P_4 \rangle$. \vec{n} is found using the numerical recipe reported in [38] which yields two orthogonal directors, \vec{n}_1 , \vec{n}_2 and the corresponding values of $\langle P_{41} \rangle$, $\langle P_{42} \rangle$ in decreasing order of magnitude, used to gauge the in-plane and out-plane alignment of the flipped and unflipped particles.

3.2. Bond orientational order parameter

The local n -fold bond orientational order, $\Phi_n(\mathbf{r}_k)$ for each k particle is given by,

$$\Phi_n(\mathbf{r}_k) = \frac{1}{N_k} \sum_{j=1}^k \exp(in\theta_{jk}) \quad (4)$$

where $i = \sqrt{-1}$ and θ_{jk} is the angle between the vector connecting particle k with its neighbor j and a fixed reference vector. N_k is the number of nearest neighbors of particles k . For $n = 6$, N_k was calculated via Voronoi tessellation, while for $n = 4$, the four closest neighbors were used to avoid the degeneracy in the Voronoi construction [39]. Note that the $\Phi_n(\mathbf{r}_k)$ are evaluated considering the center of mass coordinates of the particles projected on the 2D plane of the slit confinement.

To analyze the correlation length of the local bond order parameters, we compute the n -fold local bond orientational correlation function given by,

$$g_n(r) = \langle \Phi_n(\mathbf{0}) \Phi_n^*(\mathbf{r}) \rangle \quad (5)$$

where $*$ indicates the complex conjugate of $\Phi_n(\mathbf{r})$ for the particle at a distance r from the reference particle.

3.3. Translational and rotational mobility analysis

We tracked particle mobility by carrying out NVT ensemble simulations of the equilibrated phases at different densities with a fixed set of translation and rotation moves using fixed step size that yield acceptance probabilities between 75% and 95% to mimic pseudo diffusive particle dynamics. The translational mobility coefficient, μ_m is defined as the mean square displacement over $\Delta N_{MC,s}$ MC cycles,

$$R_s = \frac{\sum_{i=1}^N \sum_{j=0}^{N_{MC} - \Delta N_{MC,s}} |\Delta r_{(j+s,j)}^i|^2}{N(N_{MC} - \Delta N_{MC,s})} \quad (6)$$

where $\Delta r_{(j+s,j)}^i$ is the center of mass displacement of the i^{th} particle between the j^{th} and $(j + s)^{th}$ MC cycles, and N_{MC} is the total number of MC cycles in the simulation. μ_m quantifies the average in-plane local translational fluctuations for the phases under study. The rotational mobility is gauged by the autocorrelation function of particle orientation vectors over the MC cycles, defined as,

$$\theta_s = \frac{\sum_{i=1}^N \sum_{j=0}^{N_{MC} - \Delta N_{MC,s}} \vec{u}_j^i \cdot \vec{u}_{j+s}^i}{N(N_{MC} - \Delta N_{MC,s})} \quad (7)$$

where, \vec{u}^i is the principal orientation vector of particle i , and $\Delta N_{MC,s}$ is the number of MC cycles over which the axes alignment is measured. As indicated later, we rescaled ΔN_{MC} with the corresponding translational and rotational acceptance ratios and fixed step sizes, and validated the resulting mobility trends by comparing them

with those from complementary calculations with a ‘‘Dynamic’’ MC method [40].

4. Results and discussion

4.1. Brief overview of the phase diagram under hard confinement

Fig. 2 shows the quasi-2D behavior of HPs and CYLs that was mapped by tracking ϕ for different phases found at $1.74 < H^* < 1.9$ for HPs and $1.581 < H^* < 1.61$ for CYLs, where the available space only allows the formation of a monolayer. At these plate separations both HPs and CYLs can access the flipped and unflipped orientations that have distinct projected footprints on the confinement planes. The flipped HPs and CYLs cast a smaller rectangular area and hence at the highest concentrations pack into the tetratic solid (TS) and partially ordered tetratic phase which are structurally similar to those of hard rectangles at 2D-close packing [27]. The forbidden region encloses inaccessible state points at higher packing fractions due to wall overlap (see Fig. 2a and 2b) and the boundary between the TS and the forbidden region represents the packing fraction of the densest structure predicted from the Floppy Box Monte Carlo algorithm [34]. The TS is classified into Uniaxial (Uni-TS) and Biaxial (Bi-TS), based on the alignment of the orientation \vec{u} of the flipped particles. At intermediate concentrations, the unflipped orientations project a larger hexagonal and circular areas for the HPs and CYLs, respectively, thus forming 2D

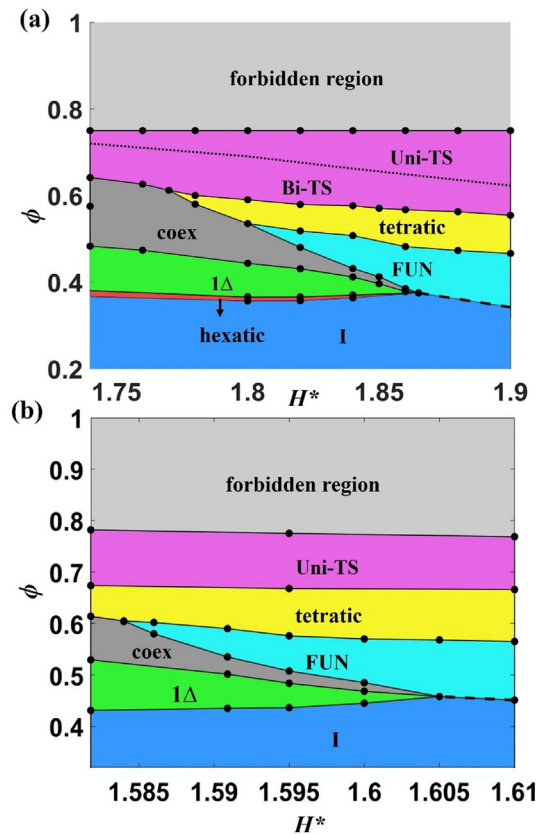


Fig. 2. Quasi-2D phase diagram for (a) HPs and (b) CYLs under hard wall confinement for varying H^* and ϕ . The dashed black line indicates a continuous boundary between the FUN and I phases. In (a) the dotted black line marks boundary between the Uni-TS and Bi-TS phases. Symbols: 1Δ = triangular solid phase, I = isotropic phase, Bi-TS = biaxial tetratic solid, Uni-TS = uniaxial tetratic solid, FUN = disordered phase with the mixture of flipped and unflipped particles, and coex = two-phase coexistence region. The forbidden region encloses inaccessible state points.

phases consistent with the assembly of hard hexagons [25] and hard disks [26]. At $1.8 < H^* < 1.865$ and $0.375 < \phi < 0.535$ for HPs and at $1.581 < H^* < 1.605$ and $0.458 < \phi < 0.614$ for CYLs, we observed an interesting re-entrant melting transition where the intervening disordered FUN phase occurs between the tetratic phase at high concentrations and the 1Δ phase at the intermediate concentrations. We observed a continuous tetratic \rightarrow FUN phase transition and a first order FUN phase \rightarrow 1Δ phase transition. The FUN phase has local clusters of flipped and unflipped particles that are randomly distributed throughout the system and the particles have relatively high translational and rotational mobility. At $H^* > 1.865$ for HPs and $H^* > 1.605$ for CYLs, the 1Δ phase disappears and the FUN phase transitions to the isotropic (I) phase upon expansion, where any ordering signature disappears as the flipped particles reached $\sim 30\%$ at the lower concentrations. The FUN phase is hence an extension of the I phase but with higher concentration of flipped particles and forms a continuous boundary with the I phase at $1.865 < H^* < 1.9$ for HPs and at $1.605 < H^* < 1.61$ for CYLs (see Fig. 2). Fig. 3 show the equilibrated snapshots, 2D structure factor plot, and \vec{u} distribution plot of the tetratic, FUN, and 1Δ phases for the HPs at $H^* = 1.84$ and CYLs at $H^* = 1.595$. The change in the structural symmetry from fourfold to disorder to hexagonal symmetry can be observed to correlate with the concentration of the flipped particles. The 2D structure factor was defined as, $S(\mathbf{k}) = \frac{1}{N} \langle \left[\sum_{i=1}^N \cos(\mathbf{k} \cdot \mathbf{r}_i) \right]^2 + \left[\sum_{i=1}^N \sin(\mathbf{k} \cdot \mathbf{r}_i) \right]^2 \rangle$, where $\mathbf{k} = (2\pi n_x/L_x, 2\pi n_y/L_y)$ with integers n_x and n_y chosen so that the wave vector \mathbf{k} corresponds to the Bragg peak for the particles position \mathbf{r}_i .

For the HPs, the hexatic and 1Δ phases occurred at $H^* > 1.74$ and $0.35 < \phi < 0.48$, where the phase regions narrow with increasing H^* and disappear at $H^* \sim 1.865$. For the CYLs, the 1Δ phase region was observed for $0.46 < \phi < 0.53$ and $H^* < 1.605$. The HPs

exhibit a 2D phase behavior for $H^* < 1.74$ and is discussed in Sec. III of the SI. We expect the CYLs to also exhibit the 2D phase behavior associated with hard disks [26] for $H^* < 1.574$.

The following section 4.2 provides a more detailed description of the characterization and properties of the different phases in Fig. 2.

4.2. Phase behavior of HPs and CYLs in hard confinement model

4.2.1. The (Uni- and Bi-) TS phases form at the highest densities

For the HPs at $\phi > 0.6$ and $1.74 < H^* < 1.9$ shown in Fig. 2a, we observed two sub-phase TS regions: Uni-TS and Bi-TS phases. The transition boundary between these phases was determined using the cubic orientational order parameters P_{41} and P_{42} [defined in Eq. (3)]. Fig. 4a shows the equation of state with P^* vs. ϕ for HPs at $H^* = 1.84$ (filled circles for compression and filled squares for expansion), where the Uni-TS phase formed at the higher concentration transitions into the Bi-TS phase upon expansion at $\phi \sim 0.662$ and $P^* \sim 12.4$. We observed a sharp drop in the values of P_{41} from 1.0 and a rise in P_{42} from 0.375 that flattens to $0.66 < P_{41} < 0.71$ and $0.62 < P_{42} < 0.63$ as the system transitions from the Uni-TS to the Bi-TS that was observed at $0.576 < \phi < 0.662$. This drop indicates that the percolating network of the orientationally aligned cluster of the flipped particles present in the Uni-TS dissolves into the Bi-TS where the size of clusters is about a few particles across and are randomly distributed along the two XY perpendicular directors (see Fig. S11 in the SI). The varying length scales of the coexisting clusters having perpendicular alignment along the XY plane suggests that the Uni-TS \leftrightarrow Bi-TS transition is continuous. The analysis using the positional pair-correlation, $g(r^*)$, and fourfold local bond orientational correlation functions, $g_4(r^*)$ [defined in Eq. (5)], shows that both Uni-TS and

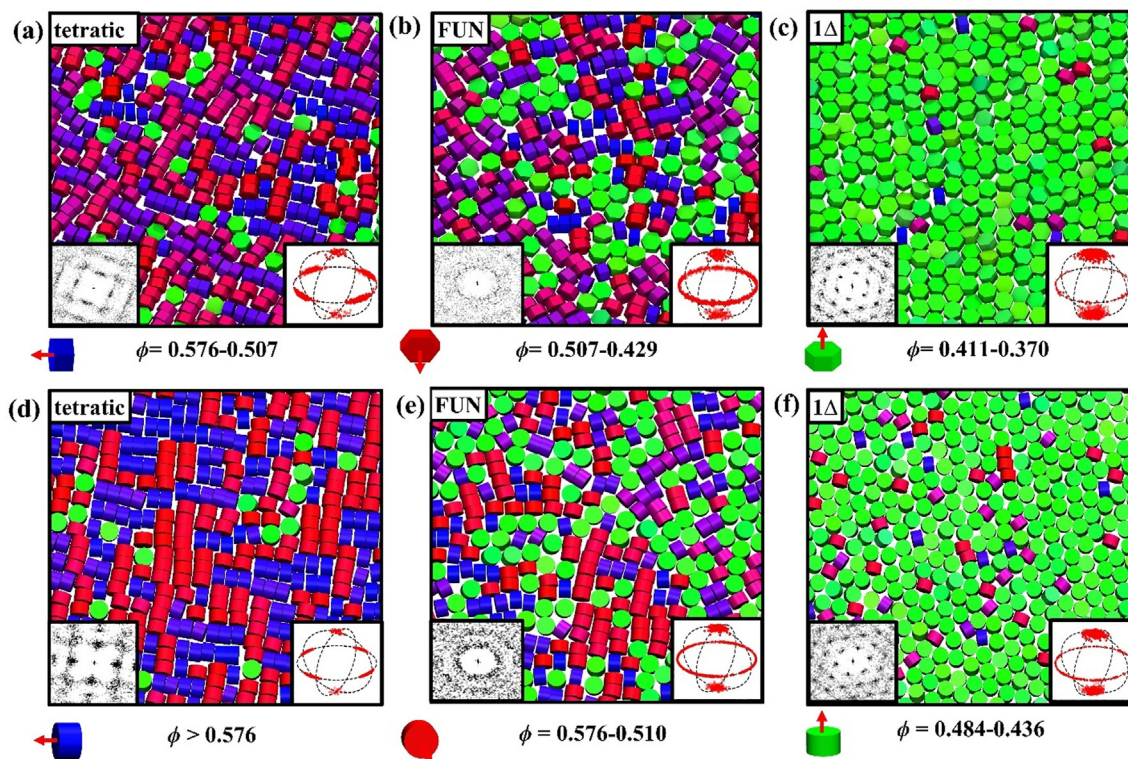


Fig. 3. Equilibrium structures of (a-c) HPs at $H^* = 1.84$ and (d-f) CYLs at $H^* = 1.595$ under hard confinement over different ranges of ϕ . Representative snapshots are shown with insets for the structure factor and \vec{u} distribution plots. Flipped particles are colored red or blue if most or least aligned with the in-plane P_4 director. Unflipped particles are colored green. Single particle \vec{u} 's are also depicted in \times axis. (For interpretation of the references to colour in this figure legend, the reader is referred to the web version of this article.)

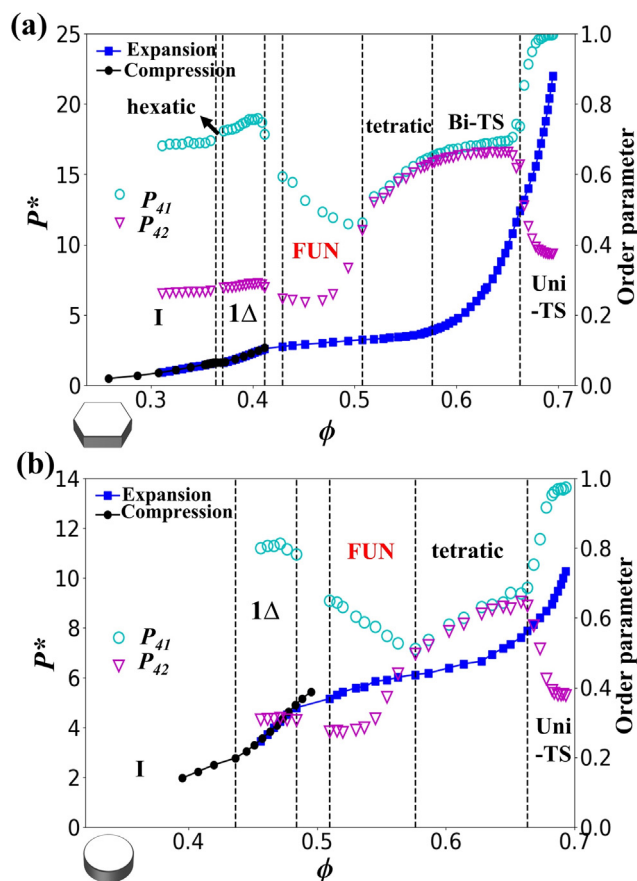


Fig. 4. Equation of state, P^* vs. ϕ , showing the compression and expansion runs for (a) HPs at $H^* = 1.84$ and (b) CYLs at $H^* = 1.595$. Dotted lines mark approximate phase boundaries. The variation of cubic order parameters P_{41} and P_{42} with ϕ is also shown. Phase symbols as in caption of Fig. 2.

Bi-TS have long-range translational and fourfold bond orientational order (see Fig. S12 and Sec. ID in the SI describing the associated square lattice structure construction). We note that the mixed bi-orientational states in the Bi-TS is stabilized by the transition between degenerate in-plane orientations of the flipped particles (sampled by the two-particle MC moves) that increases the mixing entropy, with grain boundaries contributing to increase the local free-volume. At higher ϕ , the free energy is minimized by enhancing the packing efficiency (manifested as $\Delta P < 0$) that drives the system to the more uniformly aligned columnar structure of the flipped particles in the Uni-TS.

For CYLs, the tetritic phase precedes the Uni-TS (see Fig. 2b) instead of the Bi-TS whose inherent square lattice structure cannot be realized with the CYL aspect ratio adopted here. The Uni-TS and the tetritic phase occurred at $0.66 < \phi < 0.768$ and $0.565 < \phi < 0.674$, respectively for $1.582 < H^* < 1.61$. For the $H^* = 1.595$ case shown in Fig. 4b, the Uni-TS transitions into the tetritic phase at $\phi \sim 0.663$ and $P^* \sim 7.88$. However, the tetritic phase in the range of $0.627 < \phi < 0.663$ close to the Uni-TS \rightarrow tetritic transition boundary has P_{41} and P_{42} characteristics similar to those of the Bi-TS. For the HPs, the tetritic phase occurred at $1.77 < H^* < 1.9$ and $0.466 < \phi < 0.612$, where a continuous transition from the Bi-TS to the tetritic phase was observed upon expansion. To distinguish the tetritic phase from the Uni-TS and Bi-TS, we examined $g_4(r^*)$ and $g(r^*)$ selecting the $-1/4$ exponent value as threshold to align with the KTHNY theory prediction for the scaling parameter lower-bound for the fluid to tetritic phase transition [25]. For the tetritic phase occurring at ($H^* = 1.84$, $\phi = 0.534$) for HPs and

at ($H^* = 1.595$, $\phi = 0.627$) for CYLs, $g_4(r^*)$ reveals a long-ranged order with the exponent value $> -1/4$, while $g(r^*)$ shows short range translational order with a quick decay of peak amplitude with distance (see Figs. 5 and S13). The long-range translational order in the tetritic phase is disrupted by the delocalized defects created by the weaker alignment of the local flipped particle clusters hence lowering the values of $P_{41} < 0.66$ and $P_{42} < 0.63$ compared to the Bi-TS for HPs and the Uni-TS phase for CYLs (see Fig. 4). This misalignment of the flipped particles and associated grain boundaries creates more free volume for the unflipped particles to occupy. Upon expanding the tetritic phase to $\phi = 0.507$ for HPs and to $\phi = 0.576$ for CYLs, P_{41} and P_{42} drop to moderate values in the range 0.44–0.52 as more particles attain the unflipped orientations, further destroying the translational order and the orientational alignment of the flipped particles, while still retaining the quasi-long ranged $g_4(r^*)$ order.

4.2.2. The FUN phase reenters into the 1Δ solid on expansion

As the tetritic phase transitions to the FUN phase, the P_{41} shows an inflection at ($\phi = 0.507$, $H^* = 1.84$) for HPs and at ($\phi = 0.576$, $H^* = 1.595$) for CYLs (see Fig. 4). After the inflection point, P_{41} (or P_{42}) in the FUN phase continues to increase (or decrease) with decreasing ϕ as more particles attain the unflipped orientation that disrupts the orientational order of the flipped particles. This indicates that the disorder observed in the FUN phase occurs due to the presence of clusters of flipped and unflipped particles randomly distributed throughout the system. On further expanding the FUN phase to $\phi < 0.43$ for HPs and to $\phi < 0.510$ for CYLs, the concentration of unflipped particles increases thus forming local solid-like clusters having sixfold bond orientation order that eventually nucleate the 1Δ phase. The distribution plots of \vec{u} shown in Fig. 3 indicate that the concentration of the particles with unflipped orientation increases upon expansion. To rule out the possibility that the FUN phase is a two-phase mixed state that lies within a two-phase coexistence region having metastable tetritic and 1Δ phases with incomplete melting of solid clusters, we performed an NVT ensemble interfacial simulation at $H^* = 1.84$ and $\phi \approx 0.45$ with $N = 9600$ HPs. The initial configuration for this simulation consisted of a well-separated two-phase state within an elongated box, with the high-density Bi-TS at $\phi \approx 0.60$ at one side, and the I phase formed at low-densities at the other side. We found that regardless of the initial conditions, the interface between the two phases vanished and the system ended up forming the FUN phase (see Movie 1). The FUN phase showed short-range orientational order in $g_4(r^*)$ and $g_6(r^*)$, and short-range translational order in $g(r^*)$ that transitions to the 1Δ phase with long range $g_6(r^*)$ and pronounced peaks persisting over long distances for $g(r^*)$ which is indicative of solid-like behavior (see Figs. 5 and S13). The $g(r^*)$ function also shows an increase in the lattice spacing for the 1Δ phase compared to the tetritic phase at higher concentrations.

4.2.3. The FUN and 1Δ phases have distinct pseudo dynamical signatures

To analyze and compare the dynamical properties of the FUN phase with the tetritic and 1Δ phases, we carried out the “pseudo dynamic” Monte Carlo simulations in the NVT ensemble (see Sec. 3.3 for details). We thus obtained the translational mobility coefficient, μ_m and the rotational autocorrelation function of the particle orientation \vec{u} for the tetritic, FUN, and 1Δ phases at different ϕ values for HPs at $H^* = 1.84$ and CYLs at $H^* = 1.595$ (see Fig. 6). The μ_m values for different phases were estimated from the mean square displacement plots shown in Fig. S14 in the SI. As the system transitions from the tetritic to the FUN phase, μ_m increases and the rotational autocorrelation function of \vec{u} changes from a roughly linear to a fast exponential decay. The higher mobility in

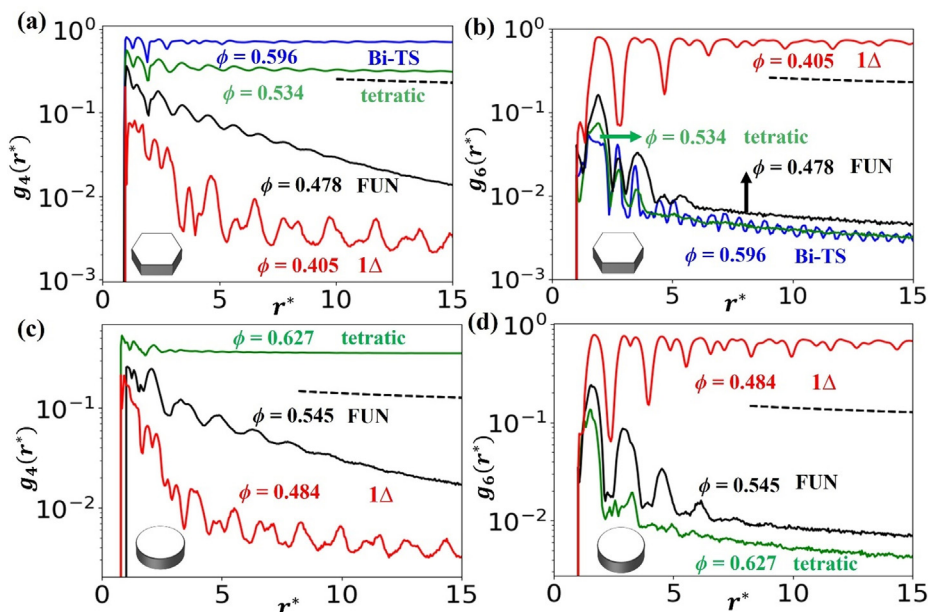


Fig. 5. Bond orientational correlation functions $g_4(r^*)$ and $g_6(r^*)$ of different phases for (a,b) 1352 HPs at $H^* = 1.84$ and (c, d) 1024 CYLs at $H^* = 1.595$ under hard confinement. r^* is the scaled radial distance. Phase symbols as in Fig. 2. The black dashed lines indicate algebraic decay of the orientational correlation with exponent $-1/4$ corresponding to the KTHNY theory prediction for the tetratic phase.

the FUN phase can be attributed to the incompatible footprint area between the flipped and unflipped particle that precludes efficient packing between local clusters. Overall, we observed that the μ_m for the FUN phase and the tetratic phase closer to the tetratic-FUN phase boundary was higher for HPs than those for CYLs, likely due to the HP facets creating more local free volume for the particles to both translate and rotate. As the FUN phase transitions to the 1 Δ phase, μ_m drops as expected, indicating that the 1 Δ phase has low XY translational mobility. The particles have higher μ_m in the I phase compared to the FUN phase for both HPs and CYLs. To compare the pseudo dynamical properties at different ϕ , we rescaled the MC step with the acceptance rates and the maximum step sizes and observed a higher translational and rotational mobility of the HPs and CYLs in the FUN phase compared to the tetratic and 1 Δ phases (see Fig. S14). We note that by fixing the maximum translational and rotational step sizes in the pseudo dynamic simulations we approximately probe differences in the local free volume available for the particle in different phases. Similar dynamic behavior for different phases (see Fig. S15) was observed by performing Dynamic Monte Carlo (DMC) simulations where the ratio between the translational and rotational step sizes were adjusted such that $\delta_t/\delta_r = \sigma_d/3 \sqrt{a_r/a_t}$ where σ_d is the diameter of the circumscribing sphere, a_r and a_t are the acceptance rates of the translational and rotational moves, respectively [40]. Although the DMC simulations provide an approximate way to study the dynamic behavior of our systems, more detailed, rigorous analysis would be required to compare the MC time scale with the Brownian time scale that couples both translational and rotational trajectories and accounts for the effects of monolayer confinement on the rotation of our biaxial particle shapes [40–43].

Interestingly, the HP 1 Δ phase at $\phi = 0.405$ reveals an exponential decay of the orientation \vec{v} (parallel to the hexagonal face) with simulation time, albeit the \vec{v} distribution shows discrete sixfold clustering due to the rotational symmetry of the hexagonal facets (see Fig. S16 in the SI). This suggests that through local coordinated motions, HPs are able to dynamically explore all the sixfold rota-

tional states despite being connected by low probability intermediate states. Accordingly, the HP 1 Δ phase can also be classified as having discrete rotator-like characteristics given the dynamic particle rotations (connecting a discrete set of orientations) which are similar to the slow hopping motions observed in the 1 Δ phase for corner-rounded hexagons [44]. We note that, in our confinement model with perfect HPs, the 1 Δ phase formed at intermediate ϕ having significant free volume to allow collective rotational and translational motions.

4.2.4. Greater confinement increases fraction of flipped particles

To understand the effect of confinement on the relative proportion of flipped and unflipped particles, we computed the variation of the fraction of flipped particles, f_f , with ϕ for different H^* values (see Fig. 7). f_f is the average fraction of particles that satisfies the criterion $|\vec{u} \cdot \vec{z}| < 0.7$ (see Sec. I in the SI). As expected, the tetratic phase has the higher proportion of flipped particles with $f_f > 0.84$ for HPs and $f_f > 0.75$ for CYLs for all plate separations. At $H^* = 1.8$ and $0.535 < \phi < 0.585$ for HPs and at $H^* = 1.582$ and $0.614 < \phi < 0.646$ for CYLs, the tetratic \rightarrow FUN phase transition disappears, and a direct tetratic \rightarrow 1 Δ phase transition occurs upon expansion (see Sec. IVD in the SI for more details). The lower density 1 Δ phase, having higher fraction of the unflipped particles with f_f ranging between 0.01 and 0.1, must be stabilized by gains in translational entropy along the z-axis (i.e., the z-translational entropy) to overcome the loss in packing entropy. In our athermal system, the associated pressure \times volume (PV) “enthalpic” contribution to the free energy acts as a knob that controls the strength of the packing entropy that optimizes local packing arrangement of the particles. At higher pressures, the free energy is minimized by enhancing the $P\Delta V < 0$ effects with the tetratic phase whose tightly packed flipped particles have low entropy associated with their restricted translational and orientational degrees of freedom. Note, however, that an efficient packing does allow gains in particle vibrational motion (and associated) entropy compared to dense but jammed configurations. The tetratic phase disappears at $H^* \sim$

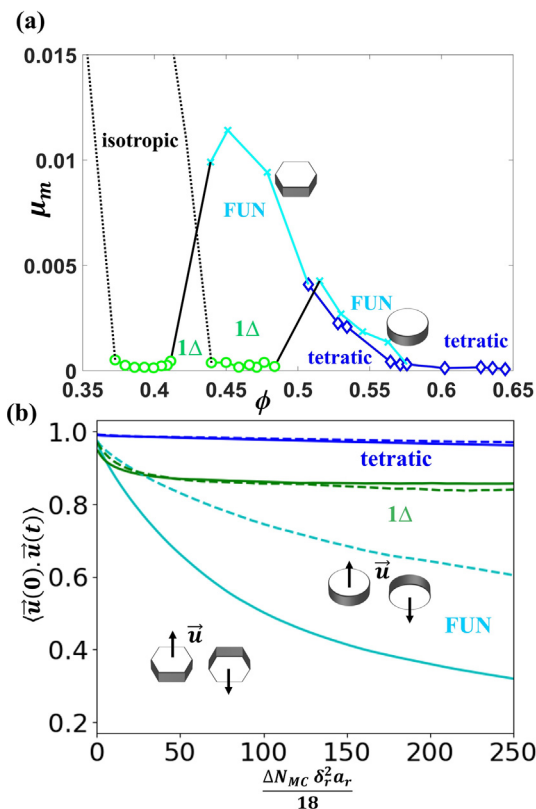


Fig. 6. Dynamic properties of the simulated phases. (a) Variation of translational mobility coefficient, μ_m with ϕ and (b) \vec{u} rotational autocorrelation function vs. rescaled Monte Carlo (MC) cycles for 1352 HPs at $H^* = 1.84$ and 1024 CYLs at $H^* = 1.595$. In (a) the coexistence region is shown as a solid black line, and the tetratic is represented with filled and open blue diamonds for the HPs and CYLs, respectively. The FUN phase is shown as cyan crosses and the 1 Δ phase as green circles. The dotted black line represents the isotropic phase. In (b) the tetratic (blue), FUN (cyan), and 1 Δ (green) phases are shown as solid lines for HPs at $\phi = 0.564, 0.478, 0.405$, and as dashed lines for CYLs at $\phi = 0.627, 0.515, 0.484$, respectively. δ_r and a_r are the rotational step size and acceptance probability, respectively. (For interpretation of the references to colour in this figure legend, the reader is referred to the web version of this article.)

1.77 for the HPs and a direct Bi-TS to 1 Δ phase transition occurs for $1.74 < H^* < 1.77$ (Fig. 2a). At higher plate separations, more free volume is available for the flipped and unflipped particles, and the FUN phase is observed for $H^* \sim 1.84$ with $0.48 < f_f < 0.85$ for HPs and for $H^* \sim 1.595$ with $0.44 < f_f < 0.76$ for CYLs. We posit that the FUN phase engenders when there is an interplay between the z-translational entropy that favors the presence of unflipped particles and the entropic packing that favors “flipped-flipped” and “unflipped-unflipped” contacts, resulting in clusters of both flipped and unflipped particles randomly distributed throughout the system. We observed a drop in the f_f values on expanding the FUN phase since the unflipped particles have then more z-translational and rotational degrees of freedom which take over the packing entropy and result in the 1 Δ phase at lower density. Figure S24 in the SI shows the increase in the spread of the z-particle distribution functions during the expansion run as the system undergoes tetratic \rightarrow FUN and tetratic \rightarrow 1 Δ phase transitions. At $H^* = 1.9$ for HPs and $H^* = 1.61$ for CYLs, the FUN phase transitions directly into the I phase upon expansion at $f_f \sim 0.3$ without crossing the stable 1 Δ phase regions, with the persistent high fraction of flipped particles impairing the formation of the 1 Δ phase. At lower concentrations, we observed a slight increase in the fraction of flipped particles in the HP hexatic phase which eventually transitions to the I phase (see Fig. 7a).

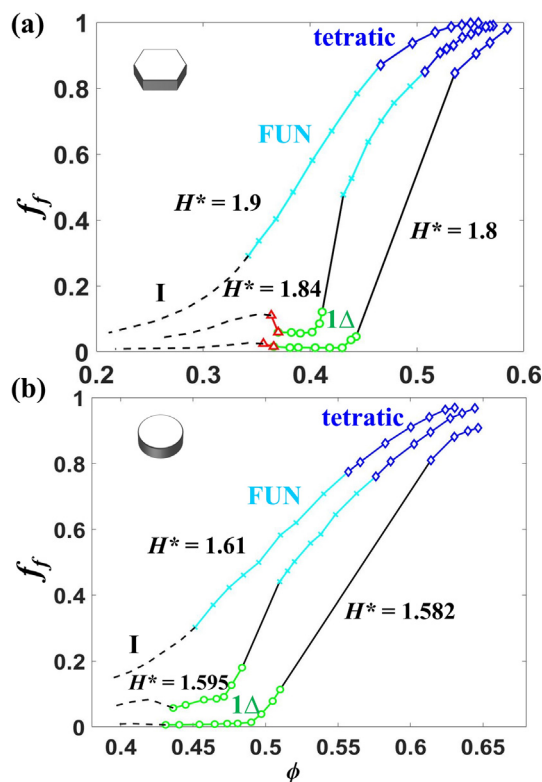


Fig. 7. Variation of the fraction of flipped particles f_f with ϕ for (a) HPs and (b) CYLs at different H^* . Solid and dashed black lines represent the coexistence region and the I phase, respectively. The tetratic, FUN, hexatic, and 1 Δ phases are represented by blue diamonds, cyan crosses, red triangles, and green circles, respectively. (For interpretation of the references to colour in this figure legend, the reader is referred to the web version of this article.)

4.3. Size polydisperse CYLs in hard confinement: Model and experiment

4.3.1. Size polydispersity can suppress 1 Δ monolayer phase and reentrant behavior

In this section, we explore the effects of size polydispersity on the re-entrant phenomenon of CYLs using MC simulations under the hard confinement model, and compare these results with experimental structures obtained from assembling the fabricated CYLs in a wedge cell confinement. The wedge cell allows us to access phases with varying concentrations of flipped particles occurring at different confinement heights. Compression runs were carried out to obtain the phases at different ϕ and H^* values for different degrees of polydispersity (see Sec. IC in the SI for simulation details). We fixed $s_\sigma = 0.06$ and $s_d = 0.01$ and 0.02 to probe whether the tetratic \rightarrow FUN \rightarrow 1 Δ phase transition is resilient to size imperfections. Note that the phase behavior at narrow plate separations is sensitive to the variation in s_d since the diameter dimension affects the fraction of particles that can access the flipped orientation observed in the FUN and tetratic phases. For $s_d = 0.02$ and $s_\sigma = 0.06$, the re-entrant phenomenon disappears and the tetratic \rightarrow FUN \rightarrow I phase transition persists (see Fig. S25 in the SI). Although the nominal s_d estimated using SEM micrographs is 0.06, the actual s_d estimated from the confocal images for the FUN phase at $\phi \sim 0.50$ was about 0.026 (see Fig. S6a in SI). This decrease in the size dispersity is likely due to the fractionation process that occurs as the particles sediment into the narrower monolayer confinement separations.

Fig. 8 shows the simulated snapshots, $S(\mathbf{k})$ plots, and the experimental confocal images for the tetratic, FUN, and 1 Δ phases for

the CYLs at different densities. The structure factor pattern changes from fourfold tetratic order \rightarrow no order \rightarrow sixfold order as the system transitions from tetratic \rightarrow FUN \rightarrow 1Δ phase. The simulated and experimental confocal images of the different phases occurred at the conditions indicated by the square and star markers in Fig. 9a that shows the variation of f_f with ϕ for CYLs with $s_d = 0.01$ and $s_\sigma = 0.06$ at different H^* . The H^* values in the simulations were chosen such that with our MC moves $>80\%$ of the particles can attain the flipped orientation at higher densities thus forming the tetratic phase. The tetratic phase was observed at $f_f > 0.75$ for $1.646 \leq H^* \leq 1.670$ (see Fig. 9a). At $H^* = 1.646$, the re-entrant FUN phase occurs at $\phi < 0.576$ and $f_f < 0.75$ and was stable up to $\phi = 0.48$ and $f_f = 0.3$ before transitioning into the 1Δ phase with $\phi = 0.46$ and $f_f = 0.08$. For $H^* > 1.646$, the 1Δ phase disappears at lower densities and the FUN phase transitions directly to the I phase. The experimental f_f values reported in Fig. 8 were obtained by manually counting the flipped and unflipped particle orientations from the confocal images with $38.6 \mu\text{m} \times 37.6 \mu\text{m}$ field area. The two orientations were distinguished based on the difference in the projected area and geometry. We estimated a total count of about 720, 620, and 540 particles in the tetratic, FUN and 1Δ phases, respectively. The volume of each particle was calculated using $\langle d \rangle$ and $\langle \sigma \rangle$ obtained from the SEM micrographs. The experimental ϕ were roughly estimated by using the average particle diameter $\langle d \rangle$ as the gap size; since the true experimental confine-

ment gap is likely greater than $\langle d \rangle$, the reported ϕ values can be seen as an upper bound for the tetratic and FUN phases. The experimental values thus estimated are $\phi \sim 0.60$ and $f_f \sim 0.94$ for the tetratic phase, $\phi \sim 0.50$ and $f_f \sim 0.74$ for the FUN phase, and $\phi \sim 0.44$ and $f_f \sim 0.06$ for the 1Δ phases. Note that the f_f value obtained for the FUN phase lies very close to the predicted tetratic-FUN phase boundary in Fig. 9a. Unflipped \leftrightarrow flipped transitions through thermal fluctuations are crucial in the experiments to access the FUN and tetratic phases. For the fabricated CYLs with dimensions $\langle d \rangle$ and $\langle \sigma \rangle$ and density mismatch $\Delta\rho$ between the solvent and the particle, we indeed estimated a barrier for unhindered unflipped \rightarrow flipped rotation to be less than k_bT (i.e., $\Delta U_g \sim 0.4 k_bT$ as shown in Sec. IIC and Fig. S6b in the SI).

4.3.2. Simulation and experimental phases have similar structural signatures

To investigate the similarities between the experimental and simulated phases, we analyzed the static and dynamic structural properties of the tetratic and FUN phases. The static properties were examined using the local orientational clustering order parameter, $P_i(r_c) = \frac{1}{n} \sum_j \cos \theta_{ij}$, where j identifies flipped particles within the distance cutoff, $r_c \sim 1.25\sigma$ from the position of the flipped particle i , n is the number of nearest neighbors, θ_{ij} is the angle between the orientations \vec{u}_i and \vec{u}_j . We set the threshold

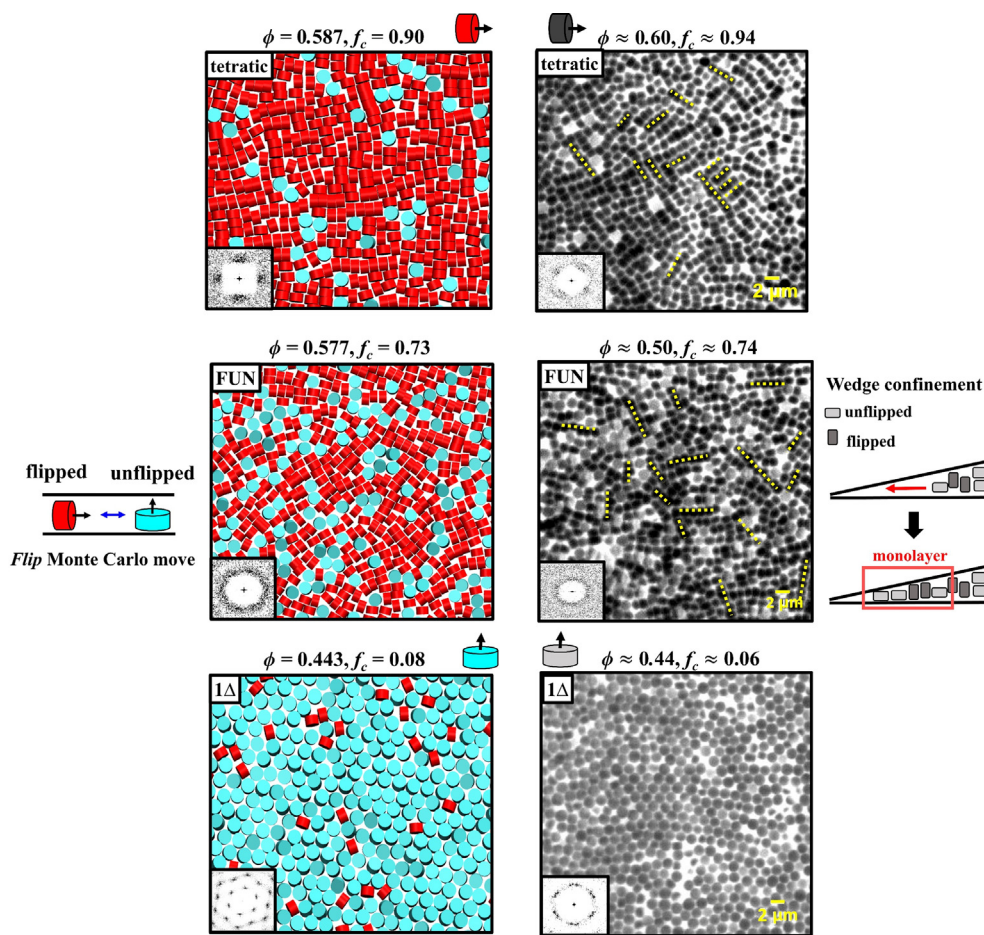


Fig. 8. Simulated (left) and confocal (right) images for CYLs under hard confinement exhibiting tetratic, FUN, and 1Δ structures with the indicated ϕ and f_f values. Insets show the structure factors. Simulated phases have $N = 1254$ and polydispersity $s_d = 0.01$ and $s_\sigma = 0.06$. Flipped and unflipped particle are colored red and cyan. (Right) The flipped and unflipped particles have different projected geometry and area. The yellow dashed lines show the local column clusters. The tetratic, FUN, and 1Δ phases have 740, 620, and 540 particles within a $38.6 \mu\text{m} \times 37.6 \mu\text{m}$ field area. Lateral schematics represent how sampling of flipped \leftrightarrow unflipped states is accomplished in MC simulations via flip moves (left) and in the wedge confinement cell via migration of flipped and unflipped particles from wide to narrow separations (right). (For interpretation of the references to colour in this figure legend, the reader is referred to the web version of this article.)

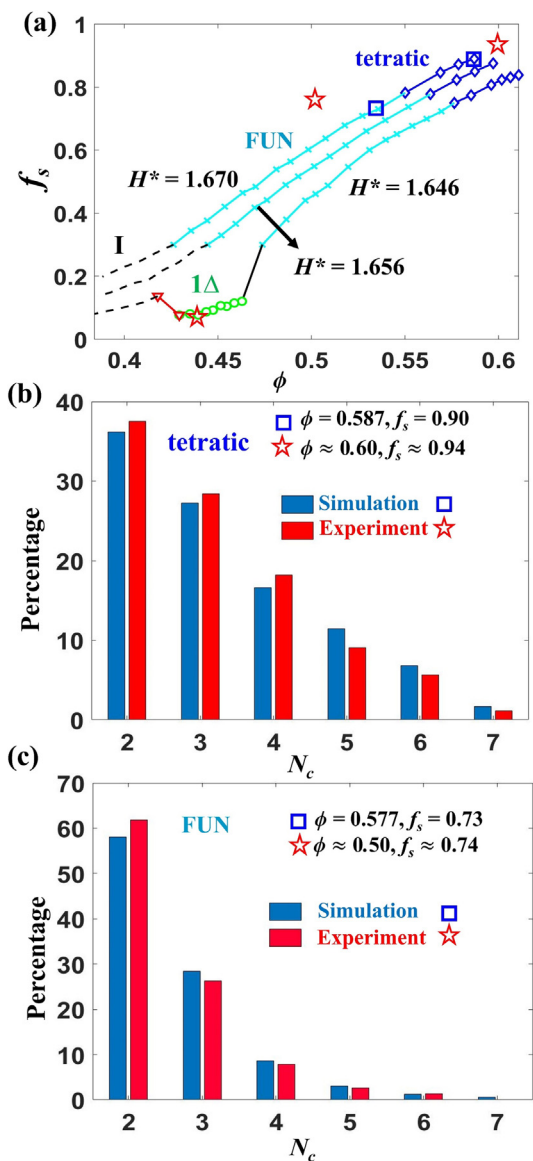


Fig. 9. (a) Variation of f_s with ϕ for CYLs with $s_d = 0.01$ and $s_h = 0.06$ at different H^* values. Black lines represent the coexistence (solid) and I phase (dashed) regions. The tetratic, FUN, hexatic, and 1Δ phases are represented by blue diamonds, cyan crosses, red triangles, and green circles, respectively. The star (red) and square (blue) markers indicate the experimental and simulated state points for the tetratic and FUN phases. (b,c) Percentage of column clusters having different number N_c of flipped particles in column stacks. (For interpretation of the references to colour in this figure legend, the reader is referred to the web version of this article.)

for $P_i(r_c)$ as 0.7 and identified the number of particles, N_c , forming a continuous network of flipped column clusters. The length of the column clusters in the confocal images were estimated by visual counting. Fig. 9b and 9c show the percentage of columns having N_c values ranging between 2 and 7 for the tetratic and FUN phases. To compare with experimental phases having similar f_s values, we used the simulated tetratic phase at $\phi = 0.587$ and $f_s = 0.90$ and the FUN phase at $\phi = 0.577$ and $f_s = 0.73$. The column length distributions from experiment and simulation agree within 10%. The tetratic/FUN phase has about 16%/8% of $N_c = 4$ columns and 9%/3% of $N_c = 5$ columns. The tetratic phase also has a higher percentage of longer columns with $N_c > 5$ and a smaller percentage of short columns with $N_c < 3$ than the FUN phase. This indicates that as f_s decreases from 0.90 to 0.73 the long columns found in the tetratic

phase break up into shorter columns in the FUN phase, destroying the fourfold features in the system. To probe the dynamic properties of the tetratic and FUN phases, we carried out pseudo dynamic NVT simulations and observed a slower decay in the rotational correlation function for the tetratic phase compared to the FUN phase (see Fig. S26 in the SI). Movie 2 shows the experimental tetratic phase with a well packed bi-orientational structure having more restricted rotational movement than the FUN phase shown in Movie 3, where the particles have more local free volume to rotate and translate. Note that the assemblies in Movies 2 and 3 the particle's motion exhibits Brownian characteristics.

Although the experimental and simulated structures of the FUN phase have similar static and dynamical properties, the experimental ϕ is lower, which could partially be due to the additional interparticle repulsive force created by the particle coating's negative zeta potential as reported in Sec. 2.2. Moreover, it is likely that the experimental structures examined had not reached the (denser) equilibrated ϕ and could be kinetically arrested. Indeed, both the 'equilibrium' FUN and tetratic phases found in simulation are only reproducibly attainable regardless of history if the particles' flipped and unflipped states are ergodically accessed, which could not have happened at the corresponding wall separations in the experiments. This indicates that the FUN and tetratic structures we observe in experiments originated when the flipped and unflipped particles occurring at wider wall separations (and lower ϕ) migrated to the narrower separations where the particles' rotational states were trapped but still had in-plane translational degrees of freedom to form more compact structures (see schematics in Fig. 8). Hence both MC simulations (with its unphysical flip moves) and the wedge-cell experiments (with its gradual narrowing and migration of large particle ensembles) provide an extensive sampling of possible particle "initial states" which can then seed dense structures that "fall" into different basins of phase space.

4.4. Bridging rotational phase space using soft-repulsive wall model

The re-entrant melting transition observed for the HPs and CYLs under the hard confinement model is associated with the broken ergodicity that results by the disconnected rotational phase space between the flipped and unflipped orientations. As an approach to dynamically bridge the gap between the two rotational states and transform the intermediate forbidden states into low-but-finite probability states, we implement a soft confinement model with a soft repulsive layer coating at the bottom wall (see Sec. 2.1 for details). By tuning the softness and thickness of a repulsive layer coating, we can control the positional penalty of the particles along the z-axis to find conditions where the reentrant phenomenon observed for the hard confinement scenario can be practically realized. We studied the phase behavior of HPs with $R = 1.82$ at $H^* = 1.95$ which allows for dynamic flipping of the particles. The phase transitions were mapped for varying values of the soft layer thickness, a^* , and its modulus parameter, β^* .

Fig. 10a shows the phase transition sequences observed for the soft confinement model at different values of soft layer parameters, β^* and a^* . The different types of phase transition sequences were identified by mapping them onto the global phase diagram for the hard wall confinement at varying H^* values shown in Fig. 2a (whose HPs have $R = 2$):

- (i) For $a^* = 0.72$ and $\beta^* < 6.5$, we observed the phase sequence corresponding to the tetratic \rightarrow FUN \rightarrow I transition. By decreasing a^* , the β^* required to attain the tetratic \rightarrow FUN \rightarrow I transition expectedly increases.
- (ii) For any value of a^* , increasing β^* pushes the phase behavior into tetratic \rightarrow FUN \rightarrow 1Δ phase transition

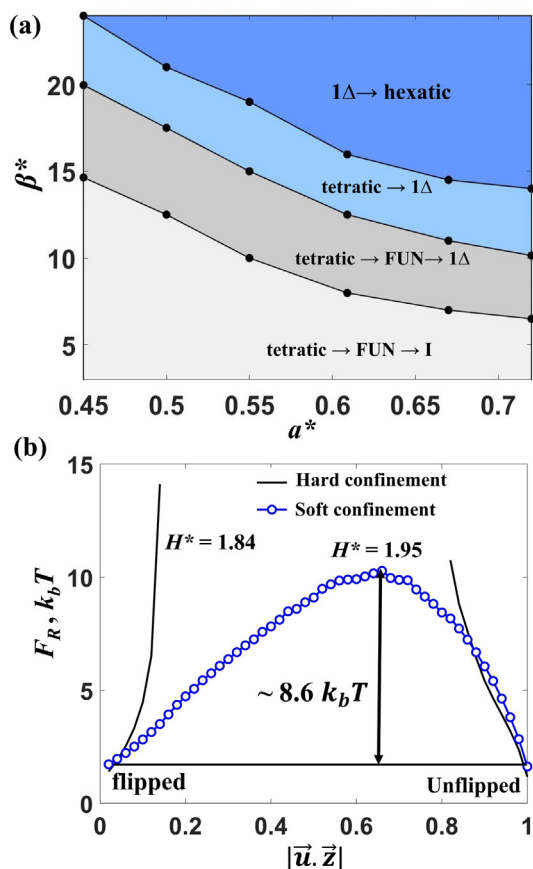


Fig. 10. (a) Different types of phase transition sequences observed using soft confinement model for varying β^* and a^* . (b) Rotational free energy F_R at different rotational states for the FUN phase with $\phi = 0.439$ at $H^* = 1.84$ under hard confinement and $\phi = 0.432$ at $H^* = 1.95$, $\beta^* = 17.3$ and $a^* = 0.45$ under soft confinement. \vec{u} is the unit vector perpendicular to the flat particle face and \vec{z} is the unit vector in the z direction.

- (iii) Further increasing β^* leads to a direct tetratic \rightarrow 1Δ transition. Figure S27 in SI shows the equation of state and the correlation functions for $a^* = 0.45$ and $\beta^* = 17.3$, where the FUN phase occurred within the range of $0.421 < \phi < 0.467$.
- (iv) Further increasing β^* leads to the $1\Delta \rightarrow$ hexatic phase transition, having 2D phase behavior since then the soft layer is rather “hard” and the effective wall separation effectively corresponds to the hard confinement model having 2D phase behavior.

To gauge if the FUN phase is dynamically accessible with the soft confinement model, we estimated the transition barrier between the unflipped and the flipped rotational states by calculating the rotational free energy, $F_R = -k_bT \ln(P(|\vec{u} \cdot \vec{z}|))$, where $P(|\vec{u} \cdot \vec{z}|)$ is the probability of occurrence of the indicated rotational state, k_b is the Boltzmann constant and T is the temperature. We compared the F_R between the hard and soft confinement models at the conditions where the intermediate FUN phase was observed; namely at $\phi = 0.432$ and $H^* = 1.84$ (see Sec. 4.2 Fig. 4) for the hard confinement model and at $\phi = 0.440$, $\beta^* = 17.3$ and $a^* = 0.45$ for the soft confinement model. Fig. 10b shows the estimated flipped \leftrightarrow unflipped particle transition barrier as $8.6 k_bT$ indicative of events with infrequent but experimentally accessible time scales of the order of 1 hr (estimated by correcting the unhindered rotational tumbling time of microparticles in water [45]). The interaction between the particles and walls and the ensuing particle-

rotation barrier can be manipulated based on the soft layer material, e.g., by tuning the grafting density and the length of grafted polymers [46,47].

4.5. Final remarks and outlook

In summary, we explored the quasi-2D (monolayer) phase behavior of hard HPs and CYLs in slit-pore confinement where the flipped and unflipped orientational states of the particles are dynamically disconnected. Phases with diverse structural order can be realized by coupling the anisotropy associated with particle shape with the restriction of the entropic degrees of freedom of these particles imposed by external potentials like slit confinement. Through specialized MC moves that ergodically sample both orientational states, our simulations mapped out the thermodynamic phase behavior. By varying the separation of the plates, one can effectively tune the z -translational entropy of the particles and hence control the fraction of particles that can access the flipped or unflipped orientations. The chosen particle shapes are such that their footprint changes significantly in area and packing symmetry (i.e., from hexagonal to tetratic) as they go from unflipped to flipped orientations. This unique combination of confinement effect and particle’s orientation creates an interesting re-entrant transition where an intervening disordered FUN phase occurs between two solid phases, namely, a tetratic phase (favored by hard rectangles) and a 1Δ phase (favored by hexagons or disks). The FUN phase has randomly distributed local clusters of flipped and unflipped particles whose incompatible footprint areas create more free volume for the particles to rearrange. The tetratic \rightarrow FUN phase transition is continuous while the FUN phase \rightarrow phase transition is first order. At narrow separations, a first order transition is observed between the tetratic phase and the 1Δ phase for both HPs and CYLs. Fast confocal image analysis of fabricated CYLs assembled at different densities inside a wedge-cell was used to identify structures consistent with the FUN phase, the 1Δ phase and the tetratic phase found by simulating particles with 1% and 6% dispersity in diameter and height, respectively. The comprehensive sampling of the accessible orientational phase space afforded by the simulations and experiments resulted in phases having similar fraction of flipped/unflipped particle states and structure, albeit at slightly different conditions. Importantly, our approaches are relevant to practical (often non-equilibrium) processes used to form materials: our simulations were able to unveil near equilibrium states that actually emerged at the end of the non-equilibrium process of filling a wedge cell with a colloidal dispersion. To illustrate alternative, close-to-equilibrium approaches that overcome the broken dynamic ergodicity inherent to the hard confinement, we also proposed a soft confinement model wherein the barrier for the flipped \leftrightarrow unflipped transition is large enough to allow the formation of the same phases seen for hard confinement, but not so large to preclude such transitions from occasionally taking place.

An alternative approach to control the flipped \leftrightarrow unflipped transitions rates and experimentally bridge the flipped and unflipped orientations would be to use a pre-programmed hard wall actuator that periodically increases and restores the original confinement gap. This time-dependent position of the hard walls could be tuned such that the fraction of time in the large separation is small enough to avoid large structural changes (like bilayer formation) but long enough to allow particle flips. Yet another approach to externally control spatial confinement is by using external electric/magnetic fields that allow for micro-manipulation of positions and orientations of electrically/magnetically active particles to drive the complex assembly of macrostructures [28,48]. The tunable external potential in the above systems enables control of the fraction of flipped/unflipped particles and can hence provide

similar conditions to reproduce the intriguing re-entrant phase behavior observed in our models. The re-entrant phase behavior unveiled in this work for the HPs and CYLs stems from the duality in the projected geometries when the orientation of a particle changes its flip state. In this context, it would be interesting to investigate how the different entropic forces responsible for the re-entrant behavior are affected by varying the aspect ratio of the particles. A re-entrant phase behavior akin to the one described in this work is likely to be associated with concomitant changes in optical properties that could be leveraged to devise photonic band gap crystals [49–51] and optical switches [52]. This unique phase behavior can also provide a template for designing reconfigurable colloidal materials where an external stimulus is used to change the confinement gap and allow the particles to access the flipped and unflipped orientations on command [53,54]. Such an actuator would allow to modulate the structure in the system to have six-fold, fourfold or no symmetry.

CRedit authorship contribution statement

B.P. Prajwal: Investigation, Methodology, Software, Writing – original draft. **Jen-Yu Huang:** Methodology. **Meera Ramaswamy:** Methodology. **Abraham D. Stroock:** Methodology, Writing – review & editing. **Tobias Hanrath:** Methodology, Writing – review & editing. **Itai Cohen:** Methodology, Writing – review & editing. **Fernando A. Escobedo:** Conceptualization, Funding acquisition, Methodology, Supervision, Writing – review & editing.

Declaration of Competing Interest

The authors declare that they have no known competing financial interests or personal relationships that could have appeared to influence the work reported in this paper.

Acknowledgements

Funding support from NSF award CBET-1907369 is gratefully acknowledged. IC and MR were supported in part by NSF award CBET-2010118. The authors thank Prof. Chekesha Watson and Eric Schwen for useful exchanges and to Yangyang Sun, Isabela Q. Matos, and Unmukt Gupta for valuable suggestions on the order parameter analysis. Valuable guidance from Dr. Garry Bordonaro and Dr. Beth Rhoades was received for lithoparticle fabrication. The fabrication work was performed at the Cornell NanoScale Facility, a member of the National Nanotechnology Coordinated Infrastructure (NNCI), which is supported by the National Science Foundation (Grant NNCI-2025233).

Appendix A. Supplementary material

Supplementary data to this article can be found online at <https://doi.org/10.1016/j.jcis.2021.09.073>.

References

- [1] Y.F. Lim, J.J. Choi, T. Hanrath, J. Nanomater. 2012 (2011) 1–6.
- [2] Y. Lu, Y. Yin, Z.Y. Li, Y. Xia, Nano Lett. 2 (2002) 785–788.
- [3] O.D. Velev, S. Gupta, Adv. Mater. 21 (2009) 1897–1905.
- [4] U. Agarwal, F.A. Escobedo, Nat. Mater. 10 (2011) 230–235.
- [5] S.C. Glotzer, M.J. Solomon, Nat. Mater. 6 (2007) 557–562.
- [6] D. Baranov, A. Fiore, M. Van Huis, C. Giannini, A. Falqui, U. Lafont, H. Zandbergen, M. Zanella, R. Cingolani, L. Manna, Nano Lett. 10 (2010) 743–749.
- [7] K. Yaman, C. Jeppesen, C.M. Marques, Europhys. Lett. 42 (1998) 221–226.
- [8] T. Biben, P. Bladon, D. Frenkel, J. Phys. Condens. Matter 8 (1996) 10799–10821.
- [9] A. Fortini, M. Dijkstra, J. Phys. Condens. Matter 18 (2006) L371.
- [10] M.R. Khadilkar, F.A. Escobedo, Soft Matter 12 (2016) 1506–1516.
- [11] D. Deb, A. Winkler, M.H. Yamani, M. Oettel, P. Virnau, K. Binder, J. Chem. Phys. 134 (2011) 214706–214715.
- [12] C. Avendaño, C.M. Liddell Watson, F.A. Escobedo, Soft Matter 9 (2013) 9153–9166.
- [13] K. Muangnapoh, C. Avendaño, F.A. Escobedo, C.M. Liddell Watson, Soft Matter 10 (2014) 9729–9738.
- [14] K. Whitham, T. Hanrath, J. Phys. Chem. Lett. 8 (2017) 2623–2628.
- [15] E.K. Riley, C.M. Liddell, Langmuir 26 (2010) 11648–11656.
- [16] E.G. Teich, G. Van Anders, D. Klotsa, J. Dshemuchadse, S.C. Glotzer, Proc. Natl. Acad. Sci. U. S. A. 113 (2016) E669–E678.
- [17] B. De Nijs, S. Dussi, F. Smalenburg, J.D. Meeldijk, D.J. Groenendijk, L. Filion, A. Imhof, A. Van Blaaderen, M. Dijkstra, Nat. Mater. 14 (2015) 56–60.
- [18] T. Geigenfeind, S. Rosenzweig, M. Schmidt, D. De Las Heras, J. Chem. Phys. 142 (2015) 174701–174714.
- [19] I.D. Hosein, C.M. Liddell, Langmuir 23 (2007) 8810–8814.
- [20] P. Gurin, S. Varga, M. González-Pinto, Y. Martínez-Ratón, E. Velasco, J. Chem. Phys. 146 (2017) 134503–134511.
- [21] S.J. Penterman, A. Singh, W.R. Zipfel, C.M. Liddell Watson, Adv. Opt. Mater. 2 (2014) 1024–1030.
- [22] K.W. Wojciechowski, D. Frenkel, A.C. Brañka, Phys. Rev. Lett. 66 (1991) 3168–3171.
- [23] S.J. Gerbode, U. Agarwal, D.C. Ong, C.M. Liddell, F. Escobedo, I. Cohen, Phys. Rev. Lett. 105 (2010) 13–16.
- [24] D.R. Nelson, B.I. Halperin, Phys. Rev. B 19 (1979) 2457–2484.
- [25] J.A. Anderson, J. Antonaglia, J.A. Millan, M. Engel, S.C. Glotzer, Phys. Rev. X 7 (2017) 021001–021015.
- [26] E.P. Bernard, W. Krauth, Phys. Rev. Lett. 107 (2011) 1–4.
- [27] A. Donev, J. Burton, F.H. Stillinger, S. Torquato, Phys. Rev. B - Condens. Matter Mater. Phys. 73 (2006) 054109–054121.
- [28] B. Rupp, I. Torres-Díaz, X. Hua, M.A. Bevan, Langmuir 34 (2018) 2497–2504.
- [29] B. Liu, T.H. Besseling, M. Hermes, A.F. Demirörs, A. Imhof, A. Van Blaaderen, Nat. Commun. 5 (2014) 1–8.
- [30] A.C. Stelson, S.J. Penterman, C.M.L. Watson, Small 13 (2017) 1603509–1603519.
- [31] E.G. Gilbert, D.W. Johnson, S.S. Keerthi, IEEE, J. Robot. Autom. 4 (1988) 193–203.
- [32] H.L. Ong, H.C. Huang, W.M. Huin, Adv. Eng. Softw. 34 (2003) 351–356.
- [33] P.J. Schneider, D.H. Eberly, Geometric Tools for Computer Graphics, Morgan Kaufmann, San Francisco, CA, 2003.
- [34] J. De Graaf, L. Filion, M. Marechal, R. Van Roij, M. Dijkstra, J. Chem. Phys. 137 (2012) 214101–214112.
- [35] S. Badaire, C. Cottin-Bizonne, J.W. Woody, A. Yang, A.D. Stroock, J. Am. Chem. Soc. 129 (2007) 40–41.
- [36] C.J. Hernandez, T.G. Mason, J. Phys. Chem. C 111 (2007) 4477–4480.
- [37] S. Badaire, C. Cottin-Bizonne, A.D. Stroock, Langmuir 24 (2008) 11451–11463.
- [38] B.S. John, C. Juhlin, F.A. Escobedo, J. Chem. Phys. 128 (2008) 044909–044913.
- [39] M. Mazars, EPL 84 (2008) 55002–55008.
- [40] F. Romano, C. De Michele, D. Marenduzzo, E. Sanz, J. Chem. Phys. 135 (2011) 124106–124113.
- [41] A. Patti, A. Cuetos, Phys. Rev. E - Stat. Nonlinear, Soft Matter Phys. 86 (2012) 011403–011419.
- [42] E. Sanz, D. Marenduzzo, J. Chem. Phys. 132 (2010) 194102–194109.
- [43] M. Chiappini, A. Patti, M. Dijkstra, Phys. Rev. E 102 (2020) R040601–R040606.
- [44] Z. Hou, K. Zhao, Y. Zong, T.G. Mason, Phys. Rev. Mater. 3 (2019) 015601–015610.
- [45] J.M. Meijer, J.J. Crassous, Small 14 (2018) 1–12.
- [46] W.L. Chen, R. Cordero, H. Tran, C.K. Ober, Macromolecules 50 (2017) 4089–4113.
- [47] C.L. Ren, Y.Q. Ma, Phys. Rev. E - Stat. Nonlinear, Soft Matter Phys. 72 (2005) 1–7.
- [48] R. Niu, C.X. Du, E. Esposito, J. Ng, M.P. Brenner, P.L. McEuen, I. Cohen, Proc. Natl. Acad. Sci. U. S. A. 116 (2019) 24402–24407.
- [49] K. Busch, S. John, Phys. Rev. E - Stat. Physics, Plasmas, Fluids, Relat. Interdiscip. Top. 58 (1998) 3896–3908.
- [50] E. Yablonoitch, J. Opt. Soc. Am. B 10 (1993) 283–298.
- [51] J. Teyssier, S.V. Saenko, D. Van Der Marel, M.C. Milinkovitch, Nat. Commun. 6 (2015) 1–7.
- [52] J. Ge, Y. Hu, T. Zhang, T. Huynh, Y. Yin, Langmuir 24 (2008) 3671–3680.
- [53] M. Lupkowski, F. Van Swol, J. Chem. Phys. 93 (1990) 737–745.
- [54] L.B. Krott, J.R. Bordin, J. Chem. Phys. 139 (2013) 154502–154512.